Supporting information (SI)

Delalande et al.

SI Materials and methods

Cloning and protein purification. The plasmid pTG11025 harboring cDNA for the Dp427m muscle isoform of human dystrophin (P11532) (National Center for Biotechnology Information Nucleotide Data Base NM-004006, provided by S. Braun Transgene, France) was used as a template for the PCR amplification of eight wild type fragments and the Becker deletion mutant (Table S1).

The cloning, expression and purification procedures for five of the eight fragments (R1-2, R1-3, R11-15, R23 and R20-24) have been described extensively in our previous papers (1, 2). Fragments were concentrated using centrifugal concentrators and the fragments were conditioned in Tris pH 7.5, NaCl 150 mM, EDTA 0.1 mM buffer with 2% glycerol for radiation protection (TNEG buffer). R16-17 was obtained from Nick Menhart (3) and transferred to TNEG buffer. The fragments R4-9 and R16-19 were newly cloned, expressed, purified and concentrated by following similar procedures. Both GST-tagged fragments were purified by affinity chromatography. The R4-9 fragment required an additional ion exchange chromatography step, and the R16-19 fragment required isoelectric focusing for purification followed by size exclusion chromatography. The latter fragment was very difficult to obtain in the amount required for SAXS acquisition without aggregation. The addition of 10 % acetonitrile to the TNEG buffer prevented aggregation after the last purification step; thus, SAXS acquisitions were made in the presence of acetonitrile for the R16-19 fragment.

The deletion mutant R16-21Δ45-47 was cloned, expressed and purified as previously described in detail (4). Briefly, the protein was recovered in *E. coli* in the form of inclusion bodies, was solubilized with N-lauryl-sarcosine (0.1%), and was purified by affinity chromatography followed by hydrophobic chromatography. It was concentrated in TNE buffer (5% glycerol). Size exclusion chromatography was performed at the end of the purification process for each protein before concentration. Purity was confirmed by SDS-PAGE; all proteins appeared as unique bands at the expected molecular weights. Protein concentration was calculated using the absorbance at 280 nm and the theoretical molar extinction coefficient obtained from the ProtParam server (http://web.expasy.org/protparam/).

Biochemical characterization

Circular dichroism was performed with a JASCO J-810 spectropolarimeter (Nantes, France) at a protein concentration of approximately 2.5 µM in TNE buffer. Spectra were acquired within the 200–250 nm range at 20°C with a path length of 0.2 cm. The percentage of α-helix was obtained using a

100% α-helix value of -36000 deg cm^2 $dmol^{-1}$ at 222 nm as previously described (2, 4). Thermal unfolding at 222 nm was followed by a temperature increase of 1 deg/min from 15 to 85°C. Because partial refolding after heating to 70°C was observed, indicating that denaturation was reversible, the CD signal was fitted to a two-state transition as previously described (2).
Acquisitions showed that all fragments were folded into alpha helices, as expected. The CD signal ratio observed at 208/222 nm was approximately 1, indicating that the R4-9 and R16-19 fragments were folded in coiled-coils, as previously shown for the fragments R1-2, R1-3, R11-15, R20-24, R23 and the deletion mutant R16-21Δ45-47 (2, 4).

Thermal unfolding of the R1-2, R1-3, R4-9, R11-15, R16-17, R23, R20-24 and deletion mutant R16-21Δ45-47 fragments was reported previously, and the melting temperatures ranged from 50 to 67°C (1, 2, 4). The R16-17 fragment was shown to have a melting temperature of 69.2°C (3). Melting temperatures for the two new fragments R4-9 and R16-19 were determined to be 61°C and 70°C, respectively. These values are comparable to those previously reported for R1-2, R1-3, R4-9, R11-15, R16-17 R23, R20-24 and the deletion mutant R16-21Δ45-47 fragments which range from 50°C to 69.2°C (1-4).

Small-Angle X-ray Scattering (SAXS) experiments.

SAXS measurements were conducted either at the European Synchrotron Radiation Facility (ESRF, Grenoble, France) on the ID14-eh3 beamline (sample R11-15) or at the French synchrotron SOLEIL (St. Aubin, France) on the SWING beamline (all other samples). All experiments were performed at 15°C. The purified protein solutions were centrifuged for ten minutes at 10,000 rpm prior to X-ray analysis to eliminate all aggregates, and their concentrations were then measured by UV absorption at λ=280 nm on a Thermo Scientific NanoDrop 1000 Spectrophotometer. For both set-ups, the scattering vector is defined as $q = 4\pi/\lambda \sin\theta$, where 2θ is the scattering angle.

ID14-eh3 set-up. The data were collected on a 2D Pilatus 1M detector at a distance of 2.43 m (λ= 0.933 Å). For R11-15 a series of 5 concentrations (1.1, 2.1, 4.6, 6.4 and 10.8 mg/ml) was prepared and stored at 4°C prior to injection into the SAXS capillary using an automatic liquid dispensing robot (sample changer). Ten frames of 1.5 seconds each were collected for alternating TNE buffer (Tris 20 mM at pH 7.5, NaCl 150 mM and EDTA 0.1 mM) and R11-15 protein samples at increasing concentrations, and were then averaged for each data-set after visual inspection. SAXS data were directly evaluated using the Primus software, as implemented in the ATSAS 2.3 suite (5). With the exception of a slight concentration dependence arising from particle interference in solution at low q values, the scattering profiles of all concentrations superimposed well at high q values. Also, the experimental SAXS data for all samples were linear in a Guinier plot of the low q region. These

observations indicated that the sample did not aggregate. The radius of gyration R_g for R11-15 was derived from the Guinier approximation $I(q) = I(0) \exp(-q^2R_G^2/3)$ for $qR_g < 0.8$. Data collected at high q using high protein concentrations and at low q using low protein concentrations were then merged, with the aim to minimize the particle interference occurring at low q and to maximize the signal/noise ratio at high q.

SWING set-up. All other samples data were recorded using an AVIEX170170 CCD detector at the energy of 12 keV. The detector was positioned at 1.807 to 1.845 m, and data were collected in a q-range of 0.005–0.5 $Å^{-1}$ (λ= 1.033 Å). For the constructs R1-2, R1-3, R4-9, R16-17, R16-19, R16-21Δ45-47, R23 and R20-24 a24a stock solution of each fragment was prepared at a final concentration between 8 and 15 mg/ml. A volume between 60 to 120 µl of the protein samples were injected into a size exclusion column (Bio SEC-3 300 Å, Agilent) and eluted directly into the SAXS flow-through capillary cell at a flow rate of 0.2 ml/min. .The overall SEC-SAXS setup is described elsewhere (6, 7). The elution buffer consisted of TNE supplemented with 2% glycerol and 10 % acetonitrile for R16-19 and the Becker deletion mutant. Two hundred fifty SAXS frames were collected continuously at a frame duration of 1.5 s and a dead time between frames of 0.5 s. Selected frames corresponding to the main elution peak were averaged using FOXTROT (7). One hundred frames accounting for buffer scattering were collected before the void volume. The averaged buffer scattering was then subtracted from the protein signal. SAXS curves displaying the same R_g in a R_g versus frames plot were averaged and used for further characterization (Figure S1). Data reduction to absolute units and frame averaging and subtraction were performed in FOXTROT.

SAXS data analysis

All subsequent data processing (Guinier approximation leading to R_g, D_{max}, Porod volumes and Kratky plots) and analysis steps were conducted with the Scatter (http://www.bioisis.net/) or PRIMUS software and other programs of the ATSAS suite (5). The non-aggregated state of our fragments was also inferred by plotting the R_g value of an individual frame versus the frame number, following the chromatographic elution during data acquisition with SEC-SAXS that showed a constant R_g value throughout (Figure S1). Concerning the R11-15 fragment, SAXS was acquired using several concentrations of the sample. The final SAXS curve was obtained by merging the scattering signal for low and high values of q, since R11-15 showed a concentration dependent increase of the R_g value indicating intermolecular interactions; the ideal R_g value was thus calculated by extrapolation to zero concentration (Table S2).. The distance distribution function P(r) and the maximum particle diameter (D_{MAX}) were calculated by Fourier inversion of the scattering intensity I(q). The GNOM program (8). was used to compute the distance-distribution function P(r). This approach also features the maximum dimension of the macromolecule (D_{MAX}) and offers an alternative calculation of R_g, which is based on

the entire scattering spectrum. Within a margin of error, these R_g values match those deduced from the Guinier approximation (Table S2).. D_{MAX} was chosen carefully to minimize the differences between calculated R_G results and to maximize the "total estimate," which indicates the agreement of the values of each criterion with their "ideal" values.

Scattering patterns $I(q)$ are also shown as Kratky plots, generated by plotting $q^2I(q)$ *vs.* q, to assess whether directly report all proteins are properly folded in solution (Figure S2A). Typically, a globular, structured protein exhibits a pronounced maximum (bell-shaped curve), whereas a random chain (for example, an unfolded protein) will plateau (9-11). Then, Porod-Debye plots ($q^4I(q)$ *vs.* q^4) was generated and allowed the compactness of all proteins to be highlighted (Figure S2B). Additional EOM analysis fails to compute structural models in agreement with R_g and D_{MAX} (Figure S2C).

Determination of Construct Molecular Weights. Molecular weights (MW) are generally derived from the SAXS data using the I(0) or using a protein of known concentration and MW, generally BSA Both methods need an accurate determination of the protein concentration. In our SEC-SAXS experiments conditions, the UV detector saturated and the protein concentration cannot be accurately determined. Therefore, we relied on alternative methods to control the MWs of our constructs in solution: *i.e* size-exclusion chromatography multi-angle light scattering (SEC-MALS) for two of our constructs (R1-3 and R11-15),) and the method developed by Rambo and Tainer (12) employing the volume of correlation (Vc) from the SAXS measurements for all fragments (Table S2). SEC-MALS experiments were performed with an HPLC system (Agilent) equipped with an UV detector module, coupled with light scattering (miniDAWN TreosminiDAWNTreos, Wyatt) and refractive index (Viscotek, Malvern) detectors. Refractive index increment value (dn/dc) of the proteins used to determine their molecular weight was 0.185 mL/g(ref). Data were collected using a customized Bio SEC3BioSEC3 column (Agilent) equilibrated with TN buffer (Tris 20 mM pH 7.4, NaCl 150 mM). The flow rate was 0.3 mL/min. Data were processed with the ASTRA software v6.1.4.25. The method developed by Rambo and Tainer (12) was used to assess the monomeric state of all proteins fragments.

Structural models derived from the SAXS data. Fitting procedures for form factor determination were done with the SASfit software (Figure S3) but to obtain more accurate models, we used the dummy residue modeling method implemented in GASBOR (13). This method builds *ab-initio* protein-like models (monte-carlo distribution of one particle per amino acid) with an average distance between dummy residues of 0.38 nm, corresponding to the mean value of the inter-residue distance in proteins. For comparison, the widely used DAMMIN approach computes models without *a priori* distance between the beads. Therefore, the GASBOR program improves the resolution and reliability of low-resolution protein models compared to DAMMIN. The scattering profiles were fitted to a q_{max}

= 0.45 $Å^{-1}$ for all samples(except for R16-19 and R16-21Δ45-47, q_{max} = 0.3 $Å^{-1}$). Twenty independent GASBOR searches were calculated for each scattering profile (Figure S4). The residuals between GASBOR calculations and the initial scattering curves are plotted and represent less than 4% of the signal. This approach allowed general structural features of each reconstruction to be identified and is an assessment of the consistency of *ab initio* solutions by the normalized spatial discrepancy (NSD) (13, 14).

The model with the smallest χ^2 among the twenty independent runs by GASBOR calculations was taken for each dystrophin fragment and was converted to volume grid constraints for the interactive flexible fitting procedure, as described in previous work (15). In the aim to perform efficient interactive simulations, the straight homology models obtained previously and based on a spectrin-derived structural template (16) were converted into augmented Elastic Network Models at coarse-grain resolution. The filamentous coiled-coil structure was thus stabilized through a spring network presenting a lower density in the vicinity of inter-repeat junctions (i.e. linkers). Six independent interactive flexible fitting simulations were performed in both orientations of the N-terminal and C-terminal ends toward the extremities of the low-resolution molecular shape by following the BioSpring protocol developed previously (17). All-atom reconstructions were produced through a non-interactive BioSpring molecular dynamics simulation of 20,000 steps. Finally, the twelve all-atom models obtained for each dystrophin fragment were optimized using a standard energy-minimization protocol (15). Evaluation of the atomic models was performed using the SAVES web server (http://services.mbi.ucla.edu/SAVES). The best model for each dystrophin fragment was selected from the best quality scores provided by the ERRAT, Prove and ProCheck programs and according to the lowest residual signal between scattering curve and SAXS theoretical curve calculated with the CRYSOL program (ATSAS Suite, all default parameters, except the use of 50 harmonics). An ERRAT quality factor equal or higher than 95% was obtained for R1-2, R4-9, R11-15, R16-17 and R23, this value was about 90% for R1-3 and the two R16-19 and R20-24 have factors both at 84%. Ramachandran statistics with high percent of allowed and favored residues and low percent of outlier atoms were obtained (Table S3). The number of disallowed residues was high for several fragments but these residues are all located in loops, in correlation with the lower accuracy for positioning these highly flexible regions. The selected models were analyzed using the Bendix applet available for VMD. Alpha helix curvature in the final SAXS-derived all atom models was measured (18, Figure S5). Chimera software enabled the definition of the kink amplitude between two consecutive dystrophin repeats by defining a main axis for each coiled-coil and measuring the deviation angle between them (19, Table S4). All models have been successfully deposited in the SASBDB database, an international curated repository for small angle scattering data and models (20) (http://www.sasbdb.org/, see Supporting Information).

Analysis of Hinge 3 (H3) by circular dichroism and NMR. The Hinge 3 region of human dystrophin was produced by Proteogenix (http://www.proteogenix.fr/) as a peptide of 47 residues with a molecular weight of 4933.2 Da and a purity of >95%. The sequence, as follows, contains 6 PRO, 8 THR, 6 LEU and 5 VAL residues:

```
         10          20          30          40
QPDLAPGLTT IGASPTQTVT LVTQPVVTKE TAISKLEMPS SLMLEVP
```

Circular dichroismspectra at 20°C from 185 to 260 nm were obtained at a concentration of 0.1 mg/mL in water at varying values of pH, ranging from 4.8 to 10 adjusted using HCl or NaOH. All spectra showed a negative peak at 198–200 nm, which is characteristic of a predominantly disordered secondary structure (Figure S8A). However, analysis of the CD spectra on the Dichroweb website (http://dichroweb.cryst.bbk.ac.uk/html/home.shtml) (21, 22) using the algorithm CDSSTR and the reference set3 indicates that 30% of β-strands are present, together with 45% of unordered regions and 25% of turns. The NMR spectra display amide proton resonance in a relatively narrow region centered at approximately 8.1 ppm, suggesting a random coil conformation for this peptide (Figure S8B). The weakness of the NOE connectivity (NOESY not shown) corroborates the absence of a well-defined structure for Hinge 3 in solution (Figure S8C).

Homology and *de novo* modelling of H3. Homology models used as starting structures for the interactive flexible fitting procedure were obtained as reported in our previous study on dystrophin fragments (16). Modelling of the H3 region was improved by following *de novo* structure prediction to avoid potential errors induced by poor sequence homology with putative patterns of the Protein Data Bank. The PEPfold program (http://mobyle.rpbs.univ-paris-diderot.fr/cgi-bin/portal.py?form=PEP-FOLD - forms::PEP-FOLD), as well as I-TASSER and Robetta, predicted a beta sheet arrangement for a portion of the H3 peptide, in agreement with our analysis of the CD spectra. Based on the structure evaluation of the predicted hinge models, we selected a H3 fold for the R16-21Δ45-47 BMD fragment bearing beta-strands.

Immunostaining of Dystrophin and nNOS on Becker muscular dystrophy skeletal muscle. Five BMD patients with the deletion of exons 45-47 and 1 patient as a control were studied for the immune-localization of dystrophin and nNOSμ. The five patients were followed in neuromuscular centers in France and they were symptomatic. The five patients were biopsied for diagnostic purposes after informed consent. The normal control muscle biopsy was obtained as surgical waste from orthopedic surgery of an individual without neuromuscular diseases. All biopsies were flash frozen in isopentane cooled in liquid nitrogen. For immunostaining muscle analysis, sections of tissues were performed at 8 μm on a cryostat (Leica CM3050S), fixed on glass slides. Slides were rehydrated in phosphate-buffered saline (PBS), fixed with paraformaldehyde 4% for 10

min, permeabilized with 0.5% Triton X-100 (Sigma-Aldrich) and blocked in PBS/4% bovine serum albumin/0.1% Triton X-100 for 1 h. Sections were incubated in PBS/2% BSA/0.1% Triton X-100 with the anti-nNOS (1:500), or with the anti-C-terminal dystrophin (1:500) overnight at room temperature, washed in PBS, incubated for 1 h with secondary antibodies, thoroughly washed in PBS, incubated with 4′,6′-diamidino-2-phenylindole for nuclear staining for 5 min and mounted in Fluoromount (Southern Biotech). Images were acquired using ×40 NA 1.4 objective lenses with Leica DM 2500 microscope the brightness/contrast was adjusted with Photoshop CS version 9.0.

SI figures and Tables

Table S1.The eight fragments of the dystrophin central rod domain and the Becker deletion mutant

Fragments (number of residues)	Starting residue	Ending residue	N-terminus sequence	C-terminus sequence
R1-2 (228)	338	563	*GS***E**VNLD…	…QD**I**LLKWQR
R1-3 (333)	338	668	*GS***E**VNLD…	…KSTAQISQ**A**
R4-9 (653)	718	1368	*GS***S**EIRKRLD**…**	**…**LLEQ**S**
R11-15 (515)	1461	1973	*GS***F**QKPAN…	…RLNFA**Q**
R16-17 (238)*	1984	2216	*GS*VMTEDMPLEI**S**YVP…	… EE**Q**KNILSEF*QPV*
R16-19 (429)	1994	2420	*GS***S**YVPS**…**	…LLQEL*(RAKQPD**L**)***
R23 (142)	2800	2939	*GS*LEAS**S**DQW…	…IDE**T**LERLQEL
R20-24 (574)	2469	3040	*GS***V**PALA…	…VRQLH**E**

Becker deletion mutant (number of residues)	First residue N-terminus sequence	Last residue C-terminus sequence	Residue in N-terminal of the deletion	Residue in C-terminal of the deletion	Sequence of the junction of the deletion	Molecular weight (kDa)
R16-21Δ45-47 (548)	1991 *GS*LEI**S**YVPS**…**	2694 …EE**T**HRLLQQF	2146	2305	...*WYLK*VSRA…	63.9

*Residues in **bold** indicate the start and end of the repeats according to the Winder alignment [36]. The GS in italics are residues added during cloning that remained after hydrolysis of the GST-tag by thrombin. *This construct was the kind gift of Nick Menhart [28]. **The sequence in parentheses was not cloned but is shown to indicate the end residue of the repeat R19.*

Table S2:SAXS parameters for the eight native dystrophin fragments and the mutant

	R1-2	R1-3	R4-9	R11-15	R16-17	R16-19	R20-24	R23	R16-21Δ45-47
qR_g range (*)	0.21-0.80 (46)	0.78-0.99 (11)	0.54-0.98 (11)	0.38-0.95 (22)	0.32-0.79 (29)	0.78- 0.99 (11)	0.61-0.90 (11)	0.34-0.80 (43)	0.60 to 0.95 (11)
R_g (Å) from Guinier**	29.9 ± 0.1	43.2 ± 0.1	78.6 ± 0.3	59.4 ± 0.4	31.0 ± 0.1	46.9 ± 0.6	58.6 ± 0.2	22.0 ± 0.1	62.4 ± 0.8
R_g (Å) from P(r)***	31.2	45.8	85.4	60.9	32.0	49.9	60.9	22.0	60.1
D_{max} (Å)	106	160	305	230	130	200	225	74	210
Porod volume (nm^3)	42	68	123	87	47	70	107	20	184
$MW_{expected}$ (kDa)	26.5	38.5	76.0	60.1	27.5	50.2	67.2	16.8	64.0
MW_{Porod}	26.3	42.5	76.9	54.4	29.4	43.8	66.9	12.5	115.0
MW_{Vc} (kDa)	21.1	29.1	49.1	46.6	22.8	42.4	53.9	12.7	89.1
$MW_{Vc\ real}$ (kDa)	20.6	28.1	47.9	45.9	22.2	41.1	52.2	12.7	87.5
Porod-Debye Exponent	3.9	4.0	3.8	4.0	4.0	3.3	3.9	3.9	3.4

* The number in parentheses indicates the number of points used
** Guinier approximation results in linear plots (FigureS1), allowing for the determination of R_g
*** Pair distribution function is shown in Figure1D

Table S3: Quality controls of the molecular all-atom models under SAXS-derived volume constraints

	ERRAT	PROVE	Ramachandran statistics by ProCheck			
	Quality factor	% outlier atoms	Favored	Additional allowed	Generously allowed	Disallowed
R1-2	94.8	3.9	90.8	4.9	1.9	2.4
R1-3	88.3	4.0	92.7	5.0	1.3	0.9
R4-9	96.7	3.0	87.3	8.3	1.6	2.8
R11-15	78.1	4.4	85.9	9.4	1.4	3.3
R16-17	96.5	7.4	84.2	7.7	5.0	3.2
R16-19	82.9	10.7	88.2	8.0	2.0	1.8
R20-24	84.4	7.7	74.2	14.0	6.1	5.7
R23	97.0	4.4	86.9	7.7	3.8	1.5
RΔ45-47	39.5	7.2	44.6	29.1	13.4	13.0

Table S4: Kink angles (in degree) measured between the main axes of two successive coiled-coil repeats, related to Figure 3 and 4

Fragments	R_n-R_{n+1}*	R_{n+1}-R_{n+2}	R_{n+2}-R_{n+3}	R_{n+3}-R_{n+4}	R_{n+4}-R_{n+5}
R1-2	40	-	-	-	-
R1-3	75	20	-	-	-
R4-9	40	20	35	55	20
R11-15	30	80	55	90	-
R16-17	45	-	-	-	-
R16-19	55	65	55	-	-
R20-24	40	45	65	55	-

*Coiled-coil repeat R_n is the first one of a given fragment and R_{n+1} is the following repeat.

**The angles are defined by Chimera (19). Main axis of a coiled coil is the axis of the encompassing cylinder for the three alpha-helices of a given repeat.

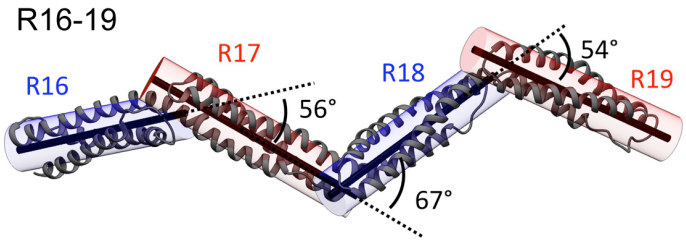

Inter-repeat kink angle measurements: the example of the R16-19 fragment model. Axis tool of the Chimera software allowed us to define a main axis for a set of atoms corresponding to dystrophin repeats in all the SAXS-derived models. Kink angles corresponding to the inter-repeat axis deviation were measured between the main axes of two consecutive repeats all along the filament.

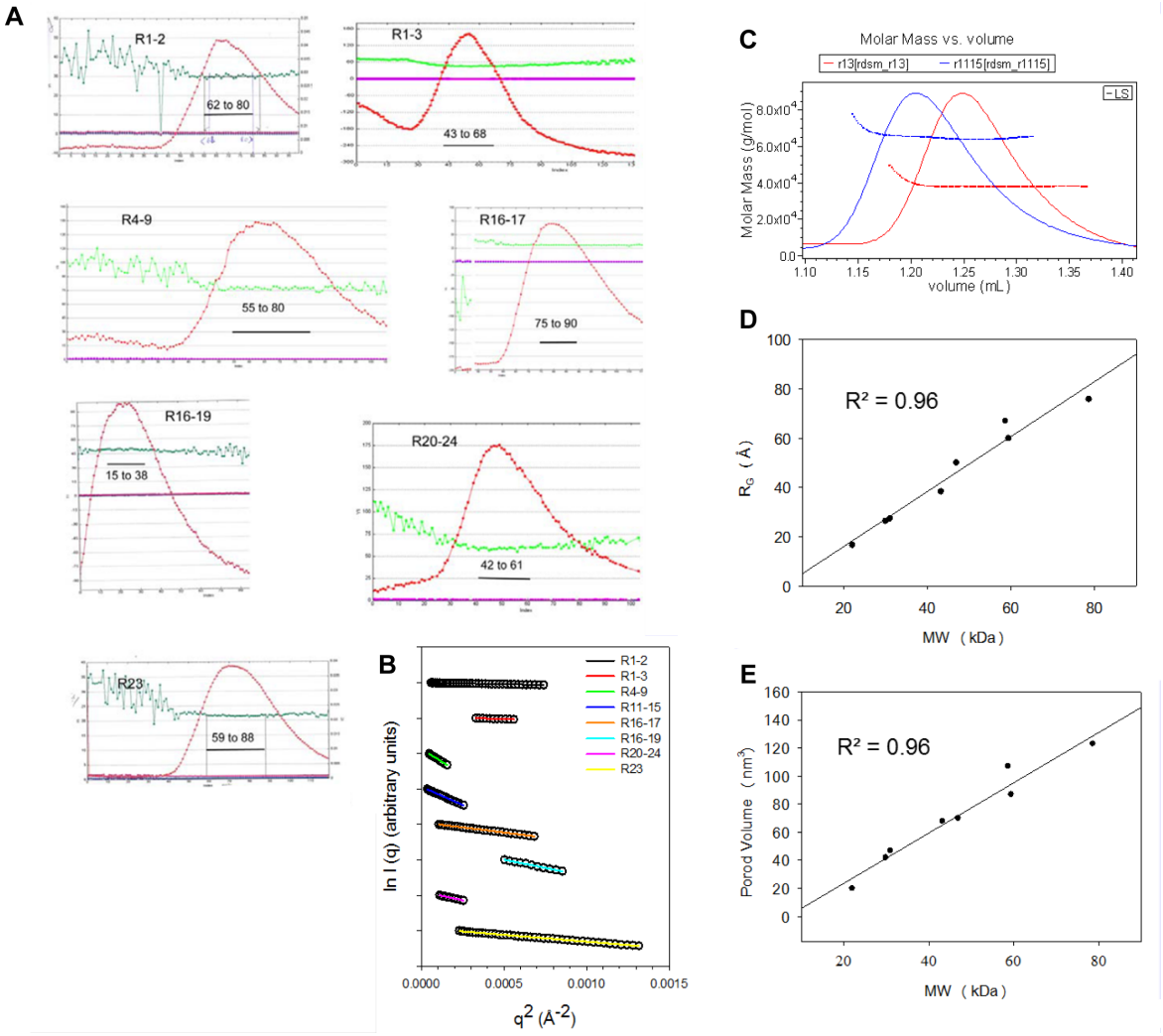

Fig. S1. Experimental SAXS data obtained for the eight distinct native dystrophin fragments. (A) R_g versus the frame number plots of the SEC-SAXS data. The scattering curves presented in figure 1 were obtained by averaging the indicated frames, (B) Guinier plots in the lowest q region of the SAXS data (the limit is defined by qRg <0.8-1.0). The plots of the eight dystrophin native fragment scattering curves are color-coded as in diagram of Figure 1A (from top to bottom: R1-2, R1-3, R4-9, R11-15, R16-17, R16-19, R20-24, and R23). (C) SEC-MALS data of R1-3 and R11-15 assessing the monomeric state of the two proteins with experimental MWs of 38.2 ± 0.1 and 65.6 ± 0.4 kDa (top of the peak), respectively. R_g (D) and Porod volumes (E) *versus* the expected MW plots for the eight protein fragments.

A. Kratky Plots

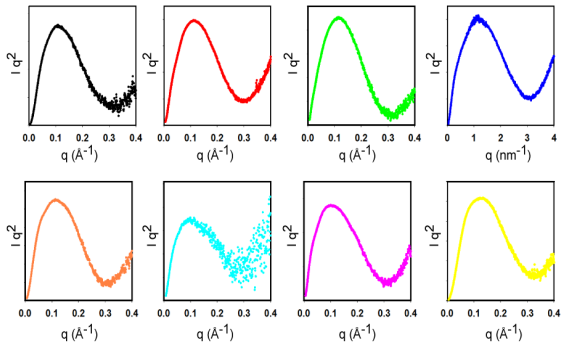

B. Porod-Debye Plots

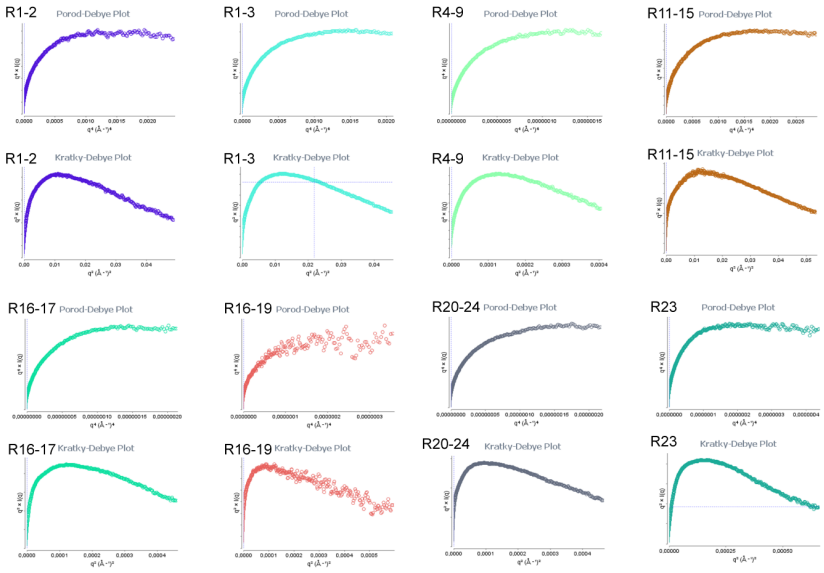

C. EOM analysis

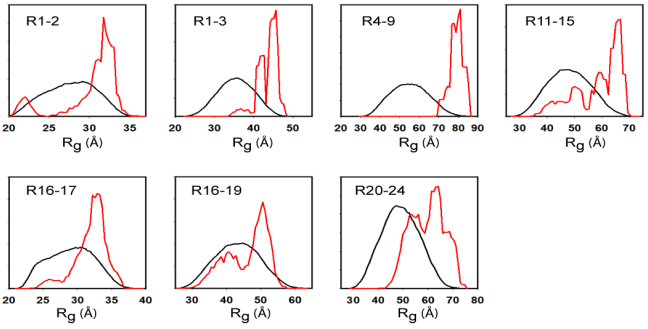

Fig. S2. (A) Kratky plots with the scattering vector S given in [Å^{-1}] for all plots except for R11-15, for which it is in [nm^{-1}]. (B) Porod-Debye and Kratky-Debye plots were obtained from the on-line server BIoIsis (http://www.bioisis.net/welcome). The plots for all fragments showed a plateau at the Porod-Debye and not at the Kratky-Debye, indicating that the fragments are more compact than flexible.(C) EOM analysis was performed through the server version of the program available online (http://www.embl-hamburg.de/biosaxs/atsas-online/). EOM is classically used to compute an ensemble of structural models in accordance to R_G and D_{MAX} obtained from analysis of SAXS data (see Table 1). This approach is particularly relevant in the case of independent subdomains separated from each other by poorly structured loop regions. In our study of dystrophin fragments, we defined as

inter-domains regions the four/eight last and four/eight first amino acids of two successive repeats. Ensembles of 10, 000 models were computed by EOM program to fit R_G and D_{MAX} parameters. Final results obtained for the seven different fragments bearing inter-repeat linkers (except the single repeat R23) were unable to propose model ensembles consistent with the SAXS-derived parameters (very low reliability chi-square values). Moreover, among the proposed models, most of them presented recurrent aberrant structural features as (i) dimeric association of two repeats and/or (ii) long range positioning of successive C-terminal amino acid of a given repeat towards the N-terminal amino acid of the following repeat. These results are in line with our proposition that repeats are modular subdomains separated by short linkers showing restricted flexibility.

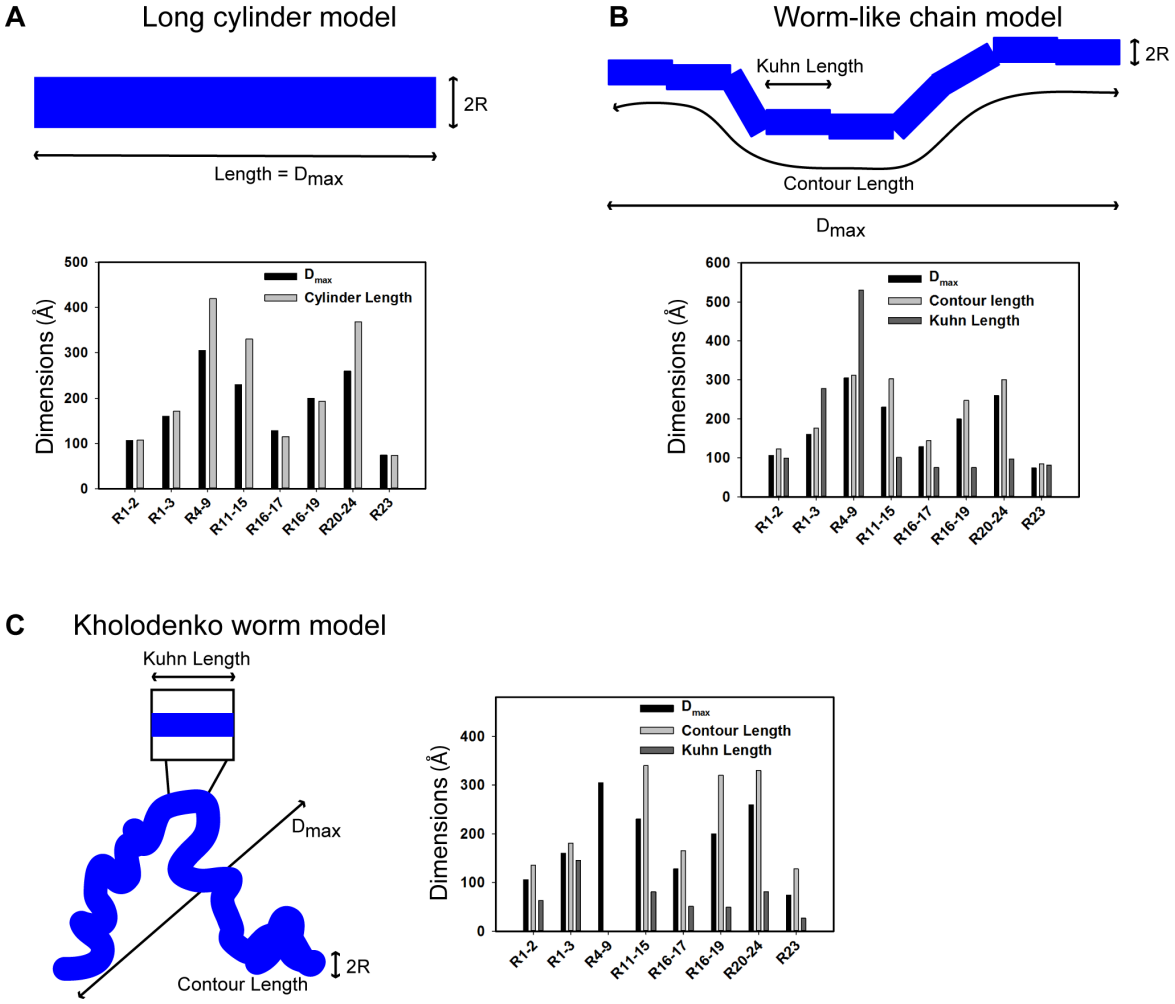

Fig. S3. **SASfit analysis of the SAXS scattering curves for the eight dystrophin fragments.**

The scattering curves were analyzed by SASFit with (A) a long cylinder model, (B) a worm-like chain model (WLCM) and (C) a Kholodenko worm model (23). The radii calculated are 12.6 ± 1 Å, 11.4 ± 0.5 Å and 10.8 ± 0.8 Å for the three models, respectively. They are all significantly different from each other ($p<0.05$). Compared to the ~10.5 Å value of the radius of the R1 crystal (24) and to the 20 Å diameter value from the P(r) distribution, the radius from the long cylinder model is ~2 Å higher and the radius from the worm-like chain model is ~1 Å higher (A and B). By contrast, the value from the Kholodenko worm model is similar to the radius of 10.5 Å calculated from the crystal structure and to the 20 Å diameter value from the P(r) (C). This agreement suggests that the Kholodenko model is more appropriate to describe the physical characteristics of our dystrophin fragments in solution as derived from their SAXS curves. The cylindrical or contour length values computed by the SASFit program for each SAXS curve were compared to the D_{MAX} obtained from the P(*r*) plot. The D_{MAX} value is actually the experimentally obtained maximum dimension of each fragment and if the fragments were pure elongated structures, there should be an adequacy between the D_{MAX} value and the cylindrical or contour lengths. The length of the long cylinder model fits with the D_{MAX} values for the shortest fragments R1-2, R1-3, R16-17, R16-19 and R23, whereas for the three other fragments, the length was longer than the D_{MAX}, showing an inadequacy of our fragments with a cylindrical model. This is confirmed by the data of the two other models, where the contour lengths are always longer than the D_{MAX}, to the exception of the computation for R4-9 fragment, which did not converge. The distortion from a cylindrical model and a contour length higher than D_{MAX} calculated by the two other models indicate that the dystrophin fragments are shorter than a theoretical linear extended rod and, consequently, should present kinks along their length. This analysis implies a molecular shape distinct from the rod-like structure previously assumed for the central domain of dystrophin (25, 26).

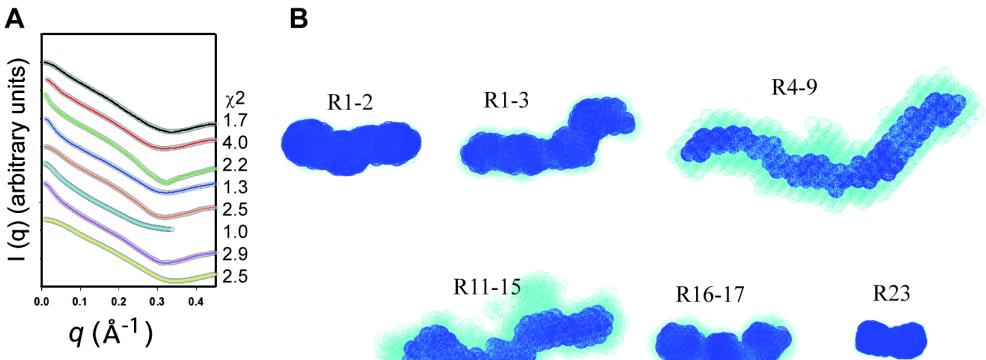

C

Fragments	NSD by DAMAVER (Å)
R1-2	0.987 ± 0.029
R1-3	1.278 ± 0.056
R4-9	1.996 ± 0.196
R11-15	2.219 ± 0.143
R16-17	0.987 ± 0.017
R16-19	1.802 ± 0.076
R20-24	2.121 ± 0.102
R23	0.8 ± 0.014

Fig. S4. Analysis of a*b initio* molecular shapes from GASBOR

(A) GASBOR fit for the *ab initio* models with the lowest χ^2 of each fragment (color-coded as in Figure 1A).(B) Twenty *ab initio* molecular shapes of the eight dystrophin fragments obtained by GASBOR program and analyzed using the ATSAS Suite (27). In light blue, the DAMAVER results corresponding to the average molecular shape after superimposition fit obtained by DAMSUP; in navy blue, the DAMFILT results allowing filtering of the averaged models. (C) Normalized spatial discrepancy (NSD) values for the 20 shapes are indicated.

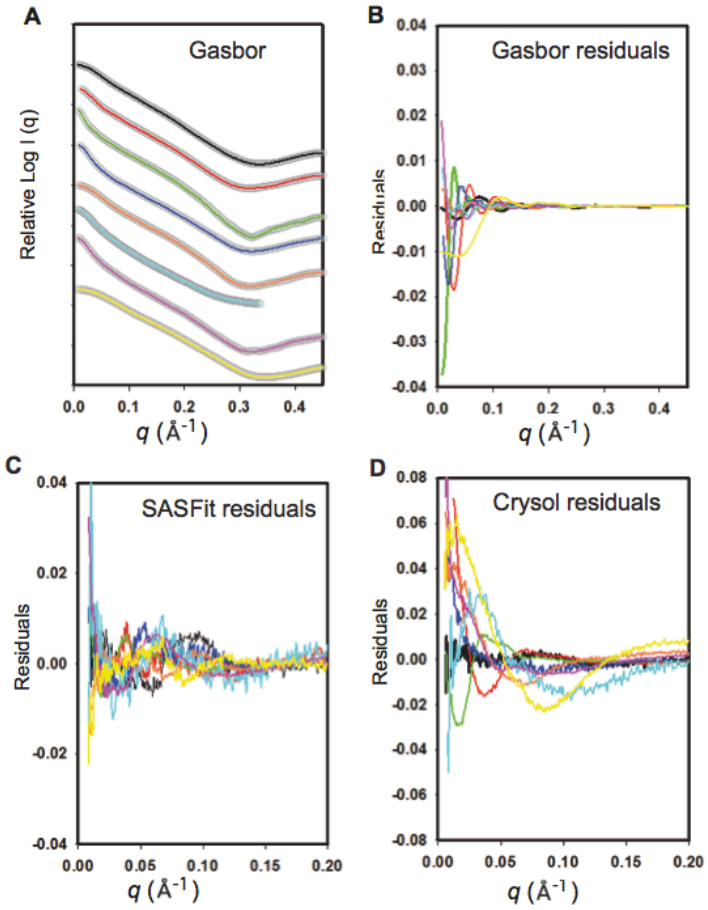

Fig. S5. Deviations between the theoretical scattering curves and the SAXS experimental curves. (A) Superimposition of theoretical curves computed for the eight native dystrophin fragments by Gasbor with the same color code as used for the Figure 1 of main text. The residuals between experimental and theoretical curves are shown for Gasbor calculations (B) and, for comparison, same residual signals are presented for SASFit calculations (C) and the Crysol calculations (D) performed on the final high-resolution models.

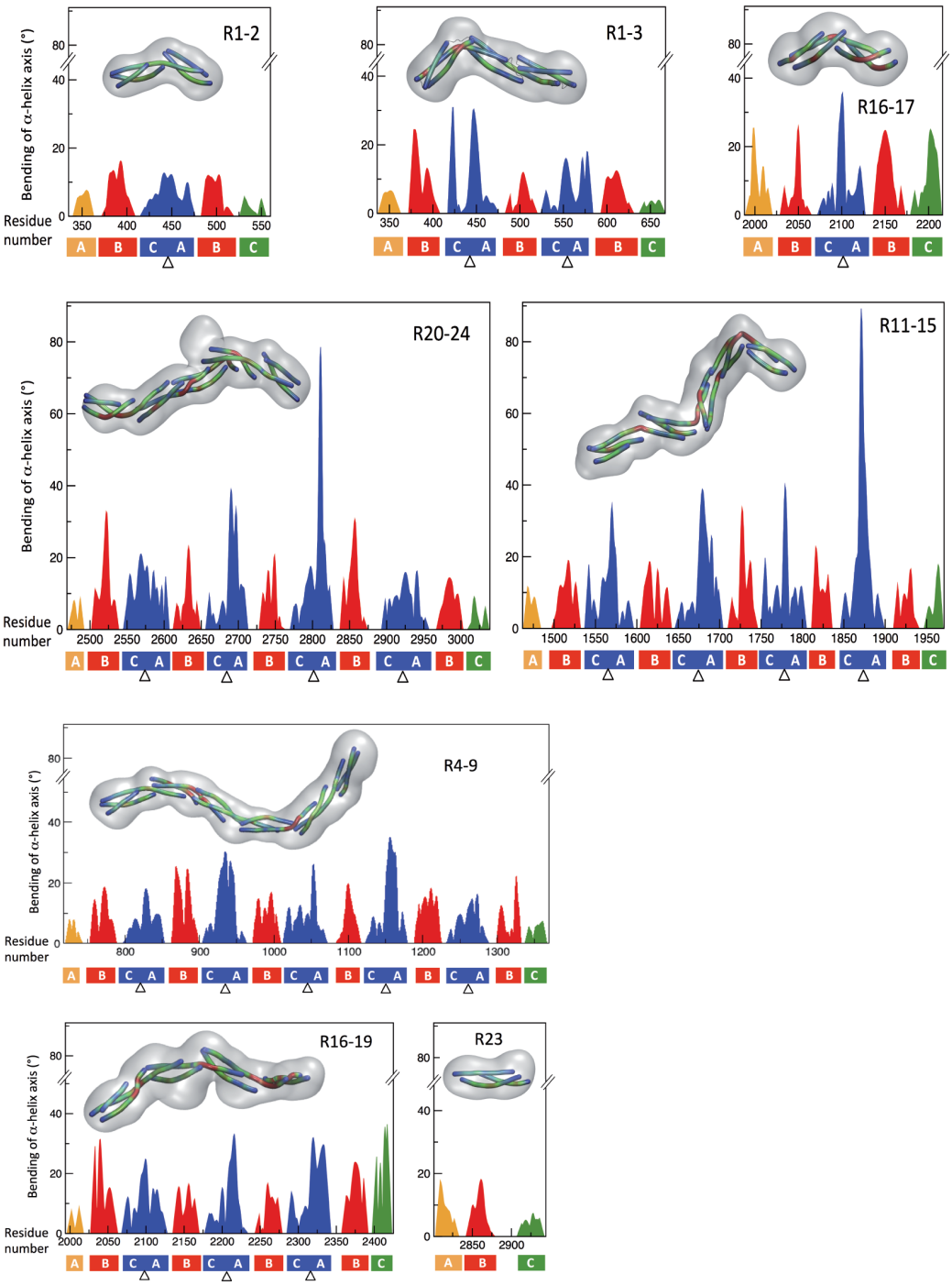

Fig. S6. Alpha helix bending analysis for all eight dystrophin fragment models
The best models obtained by SAXS-driven flexible fitting were analyzed using the Bendix (18) applet, available for VMD (28). The bending angle of alpha helices toward a straight theoretical axis was plotted (in °) according to the primary sequence of each protein. Alpha helices are indicated under the primary sequence index, and inter-repeat linkers are represented by triangles. GASBOR shapes used for the flexible fitting of dystrophin models are drawn as translucent grey volumes. Model helices are drawn as colored cylinders following their bending intensity from light (blue) to moderate (green) to strong (red) intensities.

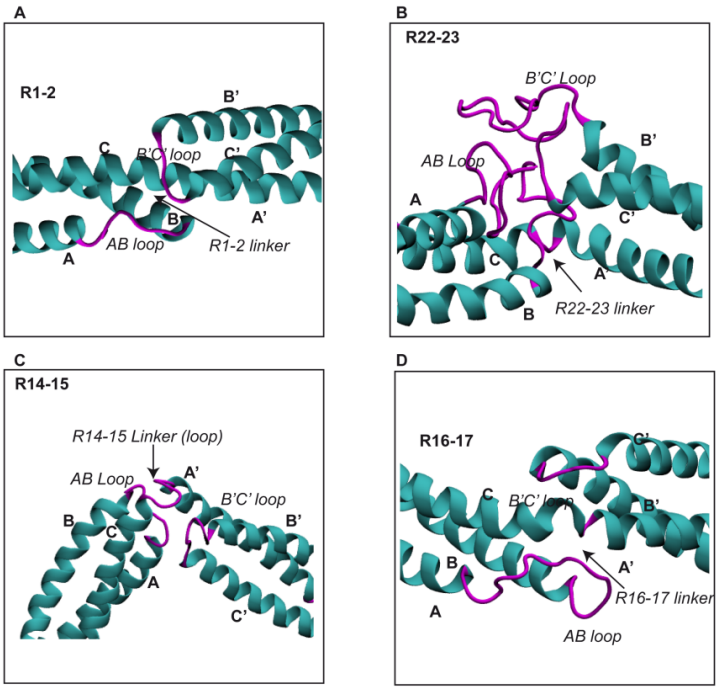

Fig. S7. Visualization of four inter-repeat linker topologies
(A) The interaction of the A/B loop of R1 with the B'/C' loop of R2 in the R1-2 model leads to a moderate kink (40°) in the linker. (B) Interaction of the long A/B and B'/C' loops of R22 and R23. (C) The linker between R14 and R15 is highly kinked and the A/B loop of R14 interacts strongly with the linker and with the B/C loop of R15 (D) A direct contact between helices B and B' is observed in the R16-17 structure that bears only a moderately kinked linker (45°), whereas no interaction between the R16 A/B loop and the R17 B'/C' loop occurs.

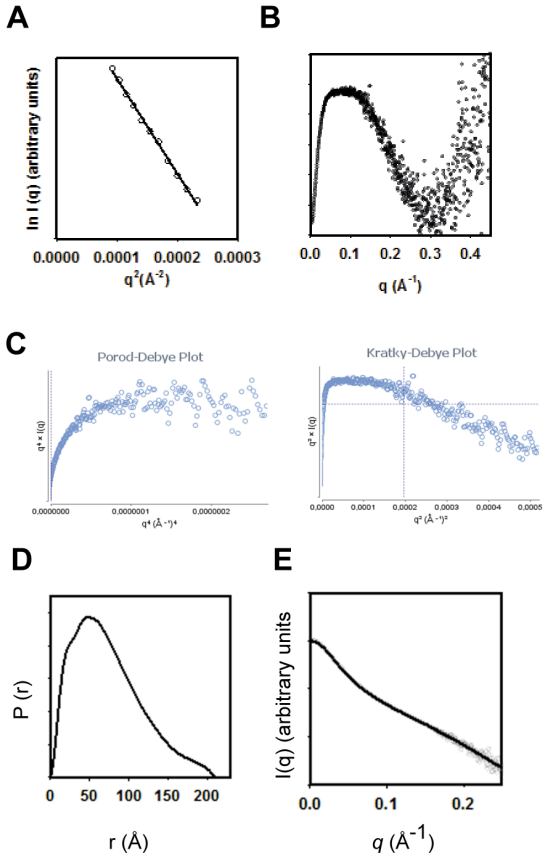

Fig. S8. SAXS-based model of the R16-21Δ45-47 deletion mutant
(A) Guinier plots in the lowest q region of the SAXS data (the limit is defined by qRg<1.0). (B) Kratky plots with the scattering vector S given in [$Å^{-1}$]. (C) Porod-Debye plot as well as Kratky-Debye plot doesn't present a clear plateau could be related to a. rather flexible protein fragment. (D) The P(*r*) distribution indicates a shoulder at a distance of 20 Å and a maximum at 48-50 Å. (E) GASBOR fit for the shape with the lowest χ^2.

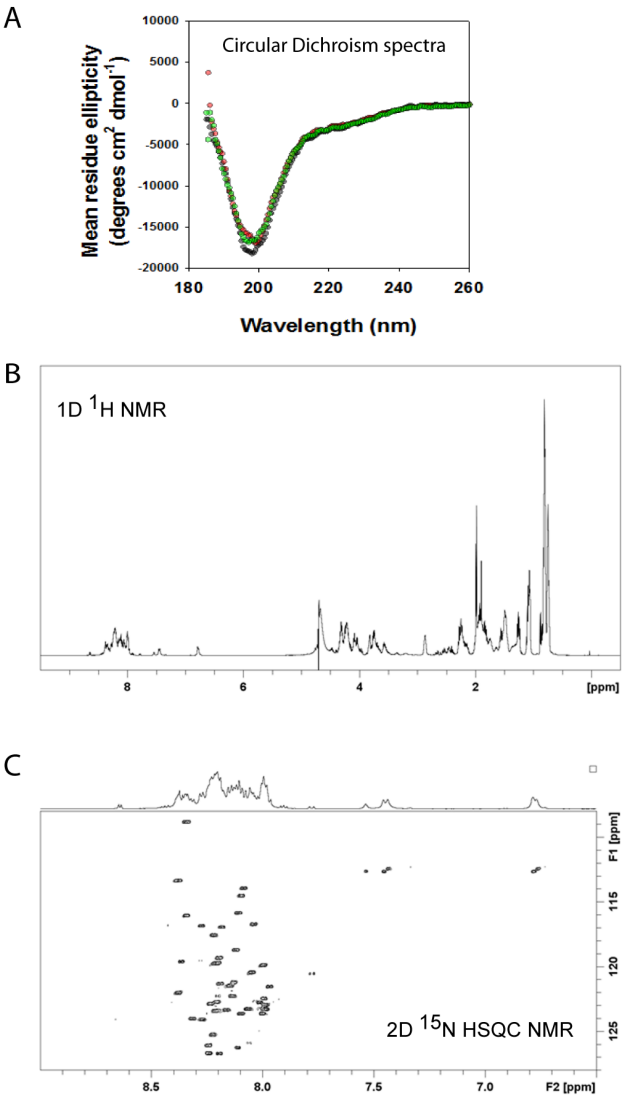

Fig. S9. Biochemical and biophysical analysis of the Hinge 3 peptide
(A) Circular Dichroism (CD) spectra of Hinge 3: the peptide concentration was 0.1 mg/mL in water and was examined at three different pH values: pH 5 (black), pH 7 (red) and pH 8.5 (green). Analysis of the spectra via the CDSSTR method using the Dichroweb server (http://dichroweb.cryst.bbk.ac.uk/html/home.shtml)(21) showed that less than 10% of the peptide is composed of alpha helix, approximately 30% of beta-strand, 25% of turns and 35% of unordered secondary structure. (B)1H–1D NMR acquisitions: NMR spectra were acquired on a Bruker Avance 500 spectrometer equipped with a 5-mm triple-resonance cryoprobe (^{1}H, ^{13}C, ^{15}N). The concentration of unlabeled protein was 15 mM at pH 4.5. (C) 2D ^{15}N-HSQC spectra were recorded at 298 K in phase-sensitive mode using the Echo anti-Echo method as matrices of 256 (t1) × 4096 (t2) complex data points; 160 scans per t 1 increment with a repetition time of 1.2 s and spectral widths of 12 and 40 ppm for ^{1}H and ^{15}N nuclei were used. Spectra were processed with Topspin (Bruker Biospin).

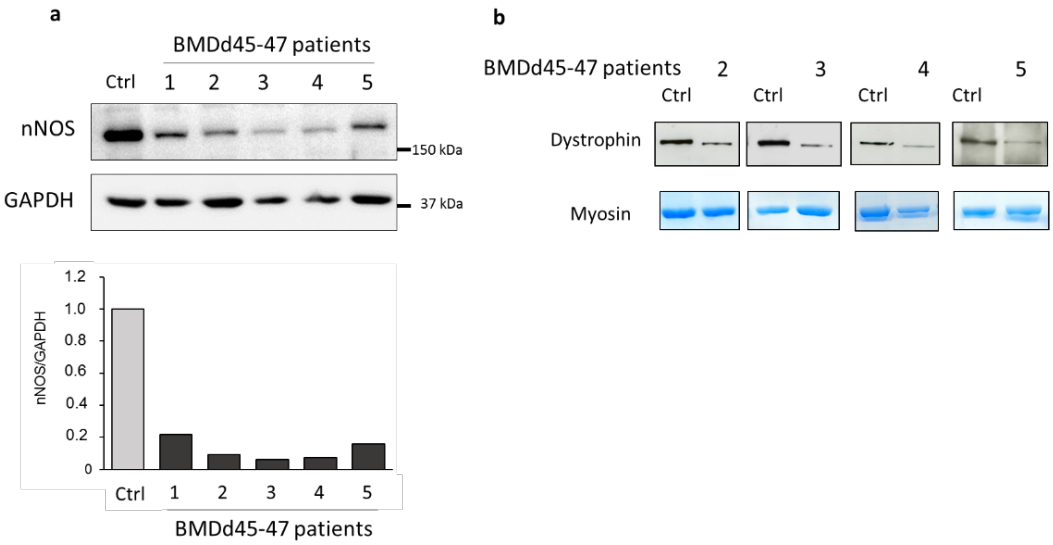

Fig. S10. nNOS and dystrophin R16-17 expression in the BMD Δ45-47 deletion mutant
(a) nNOS protein expression in healthy (Ctrl) and Becker Δ45-47 muscles, the graph represents the quantification of nNOS expression normalized to GAPDH signal by ImageJ. (b) dystrophin R16-17 expression in healthy (Ctrl) and the BMD Δ45-47 muscles and myosin expression as the protein loading control.

Supplemental video S1

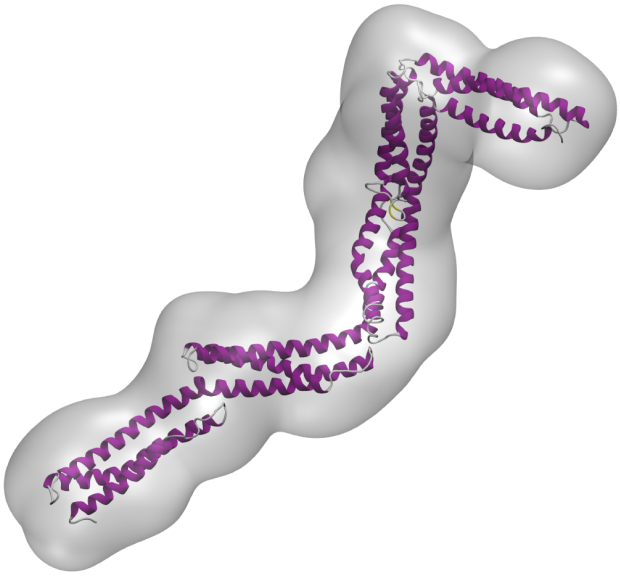

Supplemental video S1. Movie showing the reconstruction of structural models from SAXS data and molecular modelling and dynamics

References

1. Legardinier, S.*, et al.*(2008) Sub-domains of the dystrophin rod domain display contrasting lipid-binding and stability properties. *Biochim Biophys Acta* 1784, 672-682.
2. Legardinier, S.*, et al.* (2009) Mapping of the lipid-binding and stability properties of the central rod domain of human dystrophin. *J Mol Biol* 389, 546-558.
3. Mirza, A.*, et al.* (2010) A biophysical map of the dystrophin rod. *Biochim Biophys Acta* 1804, 1796-1809.
4. Nicolas, A.*, et al.* (2015) Becker muscular dystrophy severity is linked to the structure of dystrophin. *Hum Mol Genet* 24, 1267-1279.
5. Petoukhov, M. V.*, et al.* (2012) New developments in the ATSAS program package for small-angle scattering data analysis. *J Appl Cryst* 45, 342-350.
6. Perez, J. & Nishino, Y. (2012) Advances in X-ray scattering: from solution SAXS to achievements with coherent beams. *Curr Opin Struct Biol* 22, 670-678.
7. David, G. & Perez, J. (2009) Combined sampler robot and high-performance liquid chromatography: a fully automated system for biological small angle X-ray scattering experiments at the synchrotron SOLEIL SWING beamline. *J Appl Cryst* 42, 892-900.
8. Svergun, D. I. (1992) Determination of the regularization parameter in indirect-transform methods using perceptual criteria. *J Appl Cryst* 25, 495-503.
9. Koch, M. H. J., Vachette, P., &Svergun, D. I. (2003) Small angle scattering: a view on the properties, structures and structural changes of biological macromolecules in solution. *Q Rev Biophys* 36 147–227.
10. Skou, S., Gillilan, R. E., & Ando, N. (2014) Synchrotron-based small-angle X-ray scattering of proteins in solution. *Nat Protoc* 9, 1727-1739.
11. Svergun, D. I., Petoukhov, M. V., & Koch, M. H. (2001) Determination of domain structure of proteins from X-ray solution scattering. *Biophys J* 80, 2946-2953.
12. Rambo, R. P. &Tainer, J. A. (2013) Accurate assessment of mass, models and resolution by small-angle scattering. *Nature* 496, 477-481.
13. Kozin, M. B. &Svergun, D. I. (2000) A software system for rigid-bodymodelling of solution scattering data. *J Appl Cryst* 33, 775-777.
14. Volkov, V. V. &Svergun, D. I. (2003) Uniqueness of ab initio shape determination in small-angle scattering. *J Appl Cryst* 36, 860-864.
15. Molza, A.-E.*, et al.* (2014) Innovative interactive flexible docking method for multi-scale reconstruction elucidates dystrophin molecular assembly. *Faraday Discussions* 169, 45-62.
16. Legrand, B.*, et al.* (2011) Computational Study of the Human Dystrophin Repeats: Interaction Properties and Molecular Dynamics. *Plos One* 6, e23819.
17. Tek, A.*, et al.* eds. (2012) *Advances in Human-Protein Interaction - Interactive and Immersive Molecular Simulations* (InTech).
18. Dahl, A. C. E., Chavent, M., & Sansom, M. S. P. (2012) Bendix: intuitive helix geometry analysis and abstraction. *Bioinformatics* 28, 2193-2194.
19. Pettersen, E. F.*, et al.* (2004) UCSF Chimera--a visualization system for exploratory research and analysis. *J Comput Chem* 25, 1605-1612.
20. Valentini, E.*, et al.* (2015) SASBDB, a repository for biological small-angle scattering data. *Nucleic Acids Res* 43, D357-363.
21. Whitmore, L. & Wallace, B. A. (2004) DICHROWEB, an online server for protein secondary structure analyses from circular dichroism spectroscopic data. *Nucleic Acids Res* 32, W668-673.
22. Whitmore, L. & Wallace, B. A. (2008) Protein Secondary Structure Analyses from Circular Dichroism Spectroscopy: Methods and Reference Databases. *Biopolymers* 89, 392-400.
23. Kohlbrecher, J. (2010), ed. Villigen, P. S. I.
24. Muthu, M., Richardson, K. A., & Sutherland-Smith, A. J. (2012) The crystal structures of dystrophin and utrophin spectrin repeats: implications for domain boundaries. *PLoS One* 7, e40066.
25. Koenig, M., Monaco, A. P., & Kunkel, L. M. (1988) The complete sequence of dystrophin predicts a rod-shaped cytoskeletal protein. *Cell* 53, 219-226.

26. Rahimov, F. & Kunkel, L. M. (2013) The cell biology of disease: cellular and molecular mechanisms underlying muscular dystrophy. *J Cell Biol* 201, 499-510.
27. Petoukhov, M. V.*, et al.* (2012) New developments in the ATSAS program package for small-angle scattering data analysis. *J Appl Cryst* 45, 342-350.
28. Humphrey, W., Dalke, A. and Schulten, K. (1996) VMD - Visual Molecular Dynamics. *J Mol Graph* 14, 33-38.